Impact of a PEO-based Interphase at the Negative Electrode of "Zero Excess" Lithium-Metal Batteries

Katrin Geng,[1,2] Tobias Eisenmann,[1,2] Rahul Parmar,[3] Javad Rezvani,[4,5] Roberto Gunnella,[6] Matteo Amati,[3] Luca Gregoratti,[3] Dominik Stepien,[1,2,] Thomas Diemant,[1,2] and Dominic Bresser[1,2,*,z]**

[1]*Helmholtz Institute Ulm (HIU), Helmholtzstrasse 11, 89081 Ulm, Germany*
[2]*Karlsruhe Institute of Technology (KIT), 76021 Karlsruhe, Germany*
[3]*Elettra—Sincrotrone Trieste SCpA, 34149 Trieste, Italy*
[4]*INFN, Laboratori Nazionali di Frascati, Via Enrico Fermi 54, 00044 Frascati, Italy*
[5]*Consiglio Nazionale delle Ricerche (CNR), IOM-CNR, Laboratorio TASC, 34149 Trieste, Italy*
[6]*School of Science and Technology, Physics department, University of Camerino, 62032 Camerino, Italy*

"Zero-excess" lithium-metal batteries represent a very promising next-generation battery concept, enabling extremely high energy densities. However, lithium metal deposition is often non-uniform and accompanied by severe side reactions with the electrolyte, limiting Coulombic efficiency and, thus, energy density and cycle life. To address this issue, we introduced a thin polymer-based artificial interphase at the negative electrode. The influence of this interphase on the lithium deposition, and generally the reactions occurring at the negative electrode, was evaluated by galvanostatic stripping/plating tests and a thorough ex situ analysis via scanning electron microscopy (SEM) coupled with energy-dispersive X-ray spectroscopy (EDX), scanning photoemission microscopy (SPEM), and soft-X-ray absorption spectroscopy (soft-XAS). The results demonstrate that the introduction of such a polymer-based interlayer allows for more stable cycling and reduces dendritic lithium growth owing to the formation of a more homogeneous, thin, and fluorine-rich passivation layer.

Supplementary material for this article is available online

The pressing need for efficient storage of renewable energy, the ongoing electrification of the transportation sector, as well as the omnipresence of portable electronic devices in daily life underline the significance of high-energy-density batteries.[1–3] Even though the energy density of lithium-ion batteries (LIBs) has improved remarkably in the last decades, new concepts are required to significantly increase the energy density in order to meet future targets of consumers and policymakers.[4,5] "Zero excess" lithium-metal batteries (ZELMBs), also known as "anode-free" lithium-metal batteries, are considered one of the most promising beyond-LIB concepts, as they offer theoretically the highest energy density, and have, therefore, gained increasing attention very recently.[6–8] The superior energy density originates from the fact that, in the ideal case, only a current collector is employed at the negative electrode and lithium metal (characterized by a very low electrochemical potential of −3.04 V versus the standard hydrogen electrode and a theoretical specific capacity of 3860 mAh g^{-1})[9] is plated on it upon charge from the lithium-containing active material at the positive electrode—just like LIBs, but without graphite as the host structure for the lithium ions. This renders the cell setup simpler and smaller, which improves the potentially achievable gravimetric and volumetric energy density and offers the great chance to reduce cost and safety concerns.[10–12]

However, the common challenges related to lithium-metal anodes, such as the non-uniform lithium plating and low Coulombic efficiency, apply to ZELMBs as well.[13–15] In fact, these obstacles are generally even more pronounced for ZELMBs, because (i) metallic lithium is plated on a substrate different from metallic lithium and (ii) there is no lithium excess in the system to buffer the Coulombic inefficiency, thereby artificially prolonging the overall cycle life.[12] The latter is largely related to parasitic side reactions with the electrolyte and the absence of a stable solid electrolyte interphase (SEI).[13,16,17] This is not least related to the essentially infinite volume changes upon cycling, resulting in continuous fracturing and the exposure of fresh lithium surfaces, which offer new reaction sites with the electrolyte and favor inhomogeneous lithium deposition.[13,17] Therefore, a stable interphase is crucial for stable cell operation.[13,15]

There are several strategies to overcome these issues and obtain a stable SEI. The most common approach is to optimize the electrolyte composition, for example, by carefully choosing the electrolyte solvent(s),[18,19] the introduction of functional additives,[20–23] the use of highly concentrated electrolytes,[11] or dual-salt approaches.[24,25] Alternative—and potentially complementary approaches rely on the employment of 3D scaffolds at the negative electrode to homogenize the lithium deposition[26–28] and the application of thin coatings serving as artificial SEI.[15,29–31] The latter approach aims simultaneously at strengthening the in situ formed SEI, protecting the lithium surface, and facilitating a compact lithium electrodeposition.[29] Prerequisites for such an artificial interlayer are therefore high lithium-ion conductivity,[13] suitable mechanical stability,[32] and high flexibility to accommodate the volume changes,[33] while the addition of too much weight and volume to the system should be avoided. Following this approach, Hwang and co-workers[34] recently proposed a spin-coated polyethylene oxide (PEO) layer in combination with an ether-based electrolyte and 2% $LiNO_3$ as additive. They observed a remarkable average Coulombic efficiency of 95% over 100 cycles at 0.5 mA cm^{-2} with a spinning time of 90 s. In fact, PEO appears as a potentially very suitable interlayer owing to its great capability to dissolve lithium salts (for the ionic conductivity), its compatibility with metallic lithium, and low cost.[35,36] An in-depth investigation of the advantageous effect of such PEO-based artificial interphase, however, is still lacking.

Therefore, this study examines the impact of a thin PEO-based interlayer on the lithium electrodeposition on a copper current collector with a particular focus on the SEI formation in such systems via a thorough ex situ analysis. The detailed investigation of the in situ formed SEI with and without the PEO interlayer by different imaging and surface sensitive techniques—including scanning electron microscopy (SEM), scanning photoemission microscopy (SPEM) mapping (herein used for the first time in this

*Electrochemical Society Member.
**Electrochemical Society Student Member.
[z]E-mail: dominic.bresser@kit.edu

research field—to the best of our knowledge), and soft-X-ray absorption spectroscopy (soft-XAS)—allows for a better understanding of the superior performance when introducing the PEO-based artificial interphase.

Experimental

Fabrication of polymer-coated current collectors.—Thin polymer coatings on copper current collectors (Nippon) were prepared by following a solvent-free procedure similar to Kim et al.[37] PEO (Sigma-Aldrich) with an average molecular weight of 4 million g mol^{-1} was mixed with tetraethylene glycol dimethyl ether (TEGDME, Sigma-Aldrich, purity 99.9%), serving as chemically very similar plasticizer, in a 1:1 weight ratio in a dry-room (dew point of max °C–50 °C ≡ 24.1 ppm H_2O). 5 wt% benzophenone (BP, Merck, purity ⩾99%) were added as UV-crosslinking agent to enhance the mechanical stability and suppress crystallization of the PEO.[37,38] Lithium bis(trifluoromethanesulfonyl)imide (LiTFSI, 3 M) was used as conducting salt. The molar ratio of LiTFSI and the ethylene oxide units was 1:10. After homogenizing the components, the polymer was annealed overnight at 100 °C. Subsequently, the polymer was pressed on the copper current collector using a hot press (Polystat 200 T, Servitec) at 100 °C up to the maximum pressure of approx. 390 bar. The resulting membrane with a thickness of 10 μm was then placed in a UV-chamber (UVACUBE 100, Hönle UV Technology) for 6 min to initiate the crosslinking reaction.

Cell assembly and electrochemical characterization.—2032-type coin cells were assembled in an argon-filled glove box with an oxygen and water content of less than 0.1 ppm. The (surface-modified) copper current collector with a diameter of 14 mm was used as the working electrode. Lithium metal foil (Honjo) with a diameter of 12 mm and a thickness of 500 μm was used as the counter electrode. Celgard® SV718 (16 mm diameter) was used as the separator and drenched with 70 μl of the electrolyte, consisting of 85 vol% of a 1 M $LiPF_6$ solution in ethylene carbonate/dimethyl carbonate (EC/DMC, 1:1, UBE) and 15 vol% vinyl ethylene carbonate (VEC, Sigma-Aldrich).[39] Galvanostatic stripping and plating was performed at 20 °C (after equilibration for 24 h) and at a current density of 2 mA cm^{-2} (following 0.5 mA cm^{-2} for the first cycle) using a Maccor battery tester. The overall areal capacity of deposited lithium was set to 1 mAh cm^{-2}. The cut-off voltage upon stripping was set to 1.0 V.

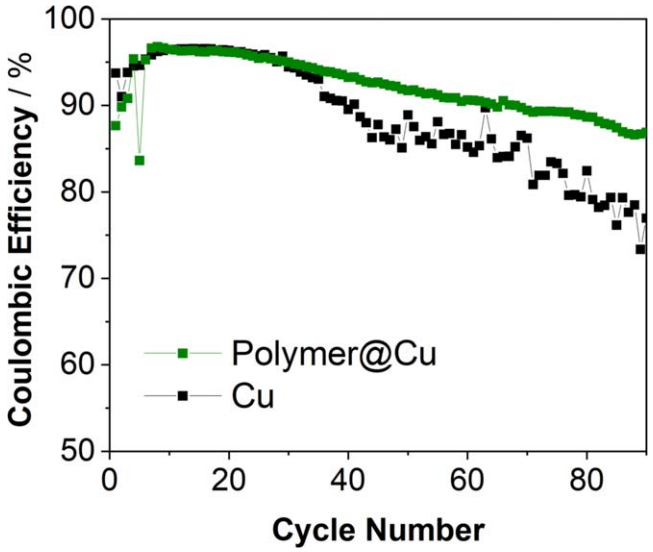

Figure 1. Coulombic efficiency of Cu||Li (in black) and Polymer@Cu||Li (in green) cells subjected to galvanostatic cycling. The cells were cycled at 2 mA cm^{-2} for 1 mAh cm^{-2} after the first cycle at 0.5 mA cm^{-2} (same areal capacity).

Physicochemical characterization.—For the ex situ analysis of cycled electrodes, the coin cells were disassembled in an argon-filled glove box using a coin cell disassembling tool (Hohsen). Since the PEO-interlayer stuck to the separator, both layers were carefully removed manually after the cells had been disassembled. Subsequently, the electrodes were washed twice with 400 μl of DMC to remove any residual liquid electrolyte. It appears noteworthy that especially in the case of the Polymer@Cu cells, when the cells were disassembled after the plating step, some of the deposited lithium stuck to the PEO-based interlayer. Thus, particular attention was paid to analyze only those parts for which we did not observe any stuck material at the PEO-based interlayer and an essentially unaffected region on the Cu foil.

Scanning electron microscopy (SEM).—SEM measurements were performed on a field emission SEM (Crossbeam X 340, ZEISS) and energy-dispersive X-ray spectroscopy (Xmax^{50} EDX detector, Oxford instruments). The SEM samples were fixed to the sample holder with conductive carbon tape. The samples were prepared inside a glovebox and transferred under argon atmosphere using an air-tight transfer box. Measurements were performed with an accelerating voltage of 5 kV and the secondary electrons were detected with an Everhart-Thornley detector. The cross-sections were obtained using a Capella FIB (gallium ion source) by milling and polishing at 30 nA and 300 pA at an accelerating voltage of 30 kV. Micrographs of the cross-sections were taken from the top and at a tilt angle of 54°. The distortion of the image caused by the tilt angle was compensated by the tilt correction of the Smart SEM software with respect to the optical axis.

Soft X-ray scanning photoemission microscopy (SPEM).—SPEM measurements were performed at the ESCA microscopy beamline of the ELETTRA synchrotron (Basovizza, Italy). The ex situ samples were handled under a constant argon overpressure before being mounted onto the stage. The excitation photon energy was fixed at 1070.9 eV throughout the experiment. The chemical maps at selected core level kinetic energies were acquired in relatively large areas between 100 × 100 μm^2 and 25.6 × 25.6 μm^2 by scanning the sample using a piezoelectric driven stage, whereas detailed core level spectra were collected at selected points/pixels with the maximum spatial resolution of around 200 nm and an energy resolution of 180 meV. All measurements were conducted at room temperature and under ultrahigh vacuum (ca. 10^{-10} mbar). The incident photon energy calibration was done using gold spectra (binding energy of Au $4f_{7/2}$ = 84.0 eV) for the XPS peak alignment. The spectra were calibrated and fitted using the CasaXPS software (Shirley-type backgrounds, peak shape: 70% Gaussian/30% Lorentzian; binding energy calibration: main C 1s peak of C–C/C–H species at 284.8 eV).

Soft X-ray absorption spectroscopy (soft-XAS).—Soft-XAS spectra were collected at the BEAR beamline of the ELETTRA synchrotron (Basovizza, Italy). The ex situ samples were handled under constant argon overpressure during the sample loading to avoid any contact with the ambient air. The spectral energy was calibrated to well-known spectral features in the simultaneously measured monitor current of the refocusing mirror. The angle of the beam with respect to the sample holder was kept at 45° for all measured spectra, and the beam had dimensions of 50 μm and 890 μm in the vertical and horizontal direction, respectively. Spectra were acquired in the total electron yield (TEY) mode and in the total fluorescence yield (TFY) mode. All spectra were normalized to the incident photon flux and calibrated using the carbon π-π^* excitation.

Results and Discussion

Figure 1 shows the comparison of the Coulombic efficiency of two cells subjected to galvanostatic cycling – one with a neat Cu foil (see Figs. S1a, S1b for a photograph and SEM micrograph) as the working electrode in black, and one with the polymer-coated Cu foil in green (Polymer@Cu, see Figs. S1c, S1d) as the working electrode (in both cases, lithium foil served as the counter electrode). The Polymer@Cu cell reaches a maximum Coulombic efficiency of around 96% within seven cycles and clearly outperforms the cell with the bare current collector after about 30 cycles. The cell with the neat Cu foil (Cu||Li) exhibits a fluctuating and strongly decreasing Coulombic efficiency starting from the 35th cycle, while the Coulombic efficiency of the Polymer@Cu||Li cell remains much more stable over the course of the following cycles. This is also reflected in the average Coulombic efficiency for the 6th to the 90th cycle, which is 92.3% for the Polymer@Cu||Li cell and only 88.3% without the polymer interlayer, revealing that the polymer interlayer enables a greater reversibility of the Li plating and stripping. This superior performance points at reduced parasitic side reactions with the electrolyte, and/or a more compact lithium deposition, and hence less dead lithium formation.

To investigate these hypotheses, in a first step, ex situ SEM images (Fig. 2) were acquired after plating 1 mAh cm ^{2} lithium at a current density of 0.5 mA cm ^{2} on the neat and polymer-coated Cu current collectors to study the morphology of the deposited lithium. The FIB-SEM cross-sections show clear differences between the lithium plated on the bare Cu current collector and the lithium plated underneath the PEO interlayer (compare Figs. 2a, 2b and Figs. 2d, 2e). Whereas the lithium plated on the neat Cu is distributed rather inhomogeneously (Figs. 2a, 2b), the lithium deposited underneath the polymer interlayer shows a relatively uniform thickness (Figs. 2d, 2e and **S2**). This substantial difference in morphology of the deposited lithium is also evident from the SEM micrographs of the surface, revealing dendritic lithium morphology in the case of the bare Cu current collector (Fig. 2c) and a much smoother denser lithium morphology in the case of Polymer@Cu (Fig. 2f). This advantageous lithium morphology favors a higher and more stable Coulombic efficiency and reversibility of the lithium plating and stripping in the long term.

After stripping all available lithium from the current collector, a clearly visible residue remained on the neat Cu current collector as revealed by ex situ SEM/EDX (Fig. 3a), covering the copper surface and consisting mainly of carbon, oxygen, and presumably lithium, while also fluorine and phosphorus were detected, though more homogeneously, as commonly expected electrolyte decomposition products. Conversely, no large mossy agglomerates were found on the copper surface of the Polymer@Cu sample after removal of the polymer interlayer (Fig. 3b). Only few particle-like residues were observed, consisting mainly of oxygen, carbon, and fluorine, suggesting the formation of lithium carbonate, lithium oxide, and lithium fluoride. This finding indicates that the incorporation of the PEO-based interlayer successfully suppresses parasitic reactions of the electrolyte with the deposited lithium metal, forming an electrochemically inactive residue on the surface.

For a more in-depth analysis of the two ex situ samples, spatially resolved XPS spectra were recorded (SPEM), yielding maps that show the elemental distribution of the elements under investigation in the uppermost surface layer (probing depth ≈2–5 nm; Figs. 4 and S3).[39] Generally, the results found for the neat copper current collector are well in line with the ex situ SEM/EDX data, revealing a pronounced formation of electrolyte decomposition products on the surface, consisting of oxygen, carbon, and lithium according to the contrast correlation, while fluorine is distributed more homogeneously (see also Fig. S3). Note that different from the SEM/EDX analysis, the SPEM method is able to detect also lithium, thus further supporting the formation of lithium carbonate and lithium oxide as decomposition products. Differently, the elemental distribution on the Polymer@Cu sample after one plating/stripping cycle is rather homogeneous (Fig. 4b), suggesting a relatively homogeneous surface coverage by the initially formed SEI beyond the PEO-based interlayer at the given sampling depth. It appears noteworthy that in both cases the samples were rinsed with DMC, thus, washing away any potentially soluble decomposition products, which would presumably also be soluble in the liquid electrolyte.

Further details on the chemical composition were extracted from the single XPS measurements at selected points of the investigated sample area (see Fig. S4). The Cu 2p detail spectra of the two measurement points on the neat Cu sample are shown in Figs. 5a, 5b. Both spectra display contributions of CuO and Cu_2O/Cu^0 (though with a very low intensity in the case of Point 1), suggesting that the SEI film formed on top is either very inhomogeneous or simply very thin, thus, allowing for the detection of these copper signals.[40] The

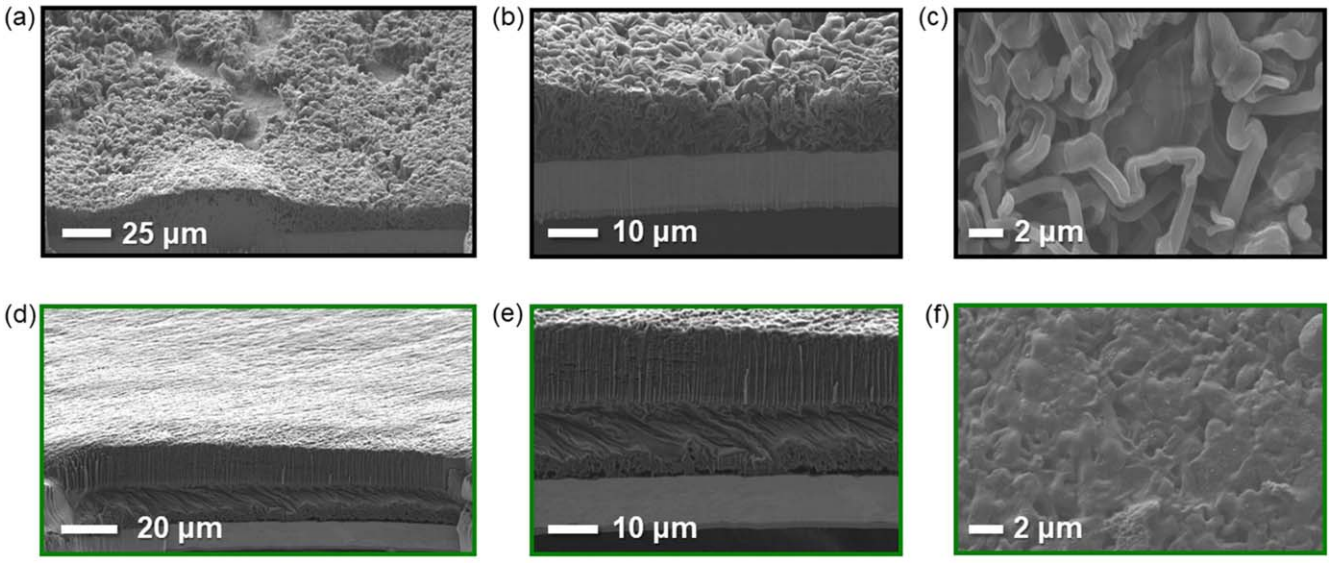

Figure 2. Ex situ analysis of the lithium deposition after plating 1 mAh cm^{-2} of lithium at 0.5 mA cm^{-2} via FIB-SEM and SEM for the (a)–(c) neat Cu current collector and (d)–(f) the Polymer@Cu: SEM micrographs of the cross-section at a (a), (d) lower and (d), (e) higher magnification; the cross-section in (b) shows the deposited lithium on the neat copper current collector, while the cross-section in (e) shows the different layers in the case of Polymer@Cu, i.e., the Celgard® separator on top of the PEO-based interlayer and beyond the deposited lithium on the copper current collector (compare Fig. S2). (c), (f) SEM micrographs of the surface morphology of the deposited lithium (the PEO-based interlayer had been carefully removed before acquiring the micrograph presented in (f)).

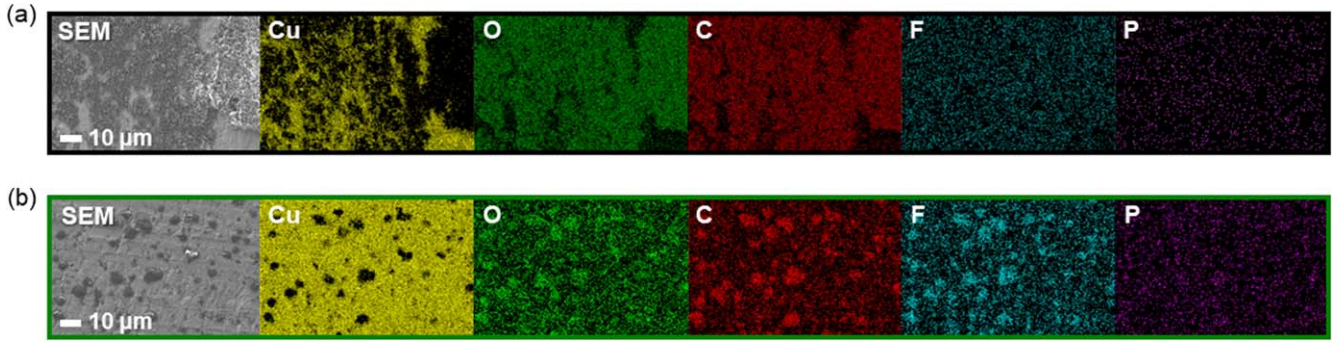

Figure 3. SEM micrographs and the corresponding EDX mapping of (a) a neat Cu current collector surface and (b) a Polymer@Cu sample after one full plating/stripping cycle (1 mAh cm^{-2} at 0.5 mA cm^{-2}). From left to right: SEM micrograph, EDX mapping of copper (in yellow), oxygen (in green), carbon (in red), fluorine (in blue), and phosphorus (in purple).

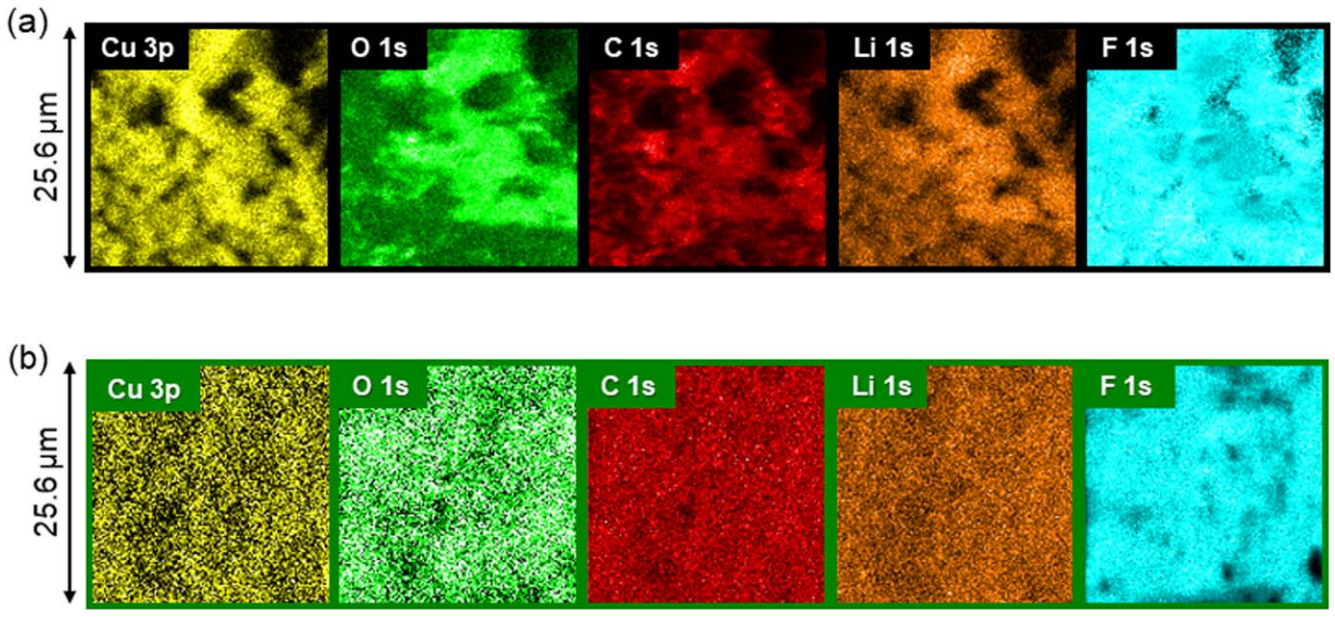

Figure 4. Spatially resolved SPEM mapping of (a) a neat copper current collector surface and (b) a Polymer@Cu surface after one full plating/stripping cycle (1 mAh cm^{-2} at 0.5 mA cm^{-2}); to be noted: the polymer interlayer was carefully removed prior to the SPEM measurements in the case of the Polymer@Cu sample. The images show the elemental distribution measured at kinetic energies of the copper 3p peak (in yellow), the oxygen 1s peak (in green), the carbon 1s peak (in red), the lithium 1s peak (in orange), and the fluorine 1s peak (in turquoise). Each pixel in the maps corresponds to one measurement at the relevant kinetic energy. The brighter the color, the higher the detected relative content of the respective element. All maps were normalized to the brightest pixel. The maps cover an area of 25.6 × 25.6 μm^2.

rather different intensity ratio of the two peaks indicates, indeed, a rather inhomogeneous SEI on the neat Cu current collector. In contrast, no Cu is detected for all three points of the Polymer@Cu sample (Figs. 5c–5e), suggesting a thicker and/or more homogeneous SEI, which is in line with the ex situ SEM/EDX and SPEM results discussed above. The O 1s detail spectra are shown in Figs. 5f–5j. The spectrum at Point 1 of the neat Cu foil (Fig. 5f) is dominated by carbonate compounds as well as lithium oxide, whereas the intensities of the CuO and Cu_2O peaks are very low in agreement with the findings for the Cu 2p region.[41–45] In contrast, for Point 2 on the neat Cu foil (Fig. 5g), the intensity of the Cu-based contributions is substantially greater, accompanied by a higher fraction of Li_2O and less organic species and Li_2CO_3. This observation indicates that the lower intensity of the copper oxides in Fig. 5f is directly related to the relatively higher intensity of electrolyte decomposition products covering the Cu current collector due to a comparably thicker (or simply more) SEI. Besides, these findings confirm the rather inhomogeneous SEI formation and composition on the neat Cu current collector. In stark contrast, the O 1s detail spectra recorded for the Polymer@Cu sample are all very similar and dominated by two main peaks that can be assigned to C-O-C and $ROCO_2Li/Li_2CO_3$ species.[41,45] These originate from the decomposition of the organic carbonates in the liquid electrolyte and, presumably, the TEGDME and PEO comprised in the artificial interphase. Besides, the peak at 531.5 eV might also contain contributions from phosphate, which were detected in the P 2p region (see Fig. S5).[46] The similarity of the spectra Figs. 5h–5j acquired at the different measurement points nicely confirms the general finding that the SEI is much more homogeneous in the case of Polymer@Cu compared to the neat Cu foil (Figs. 5f–5g). The spectra in the C 1s region (Figs. 5k–5o) basically confirm the findings from the other spectra and the SPEM data, showing peaks related to C–O–C, as well as $ROCO_2Li$ and Li_2CO_3 (compare Fig. 4).[41,45,47] The carbonate peaks and the peak assigned to poly-VEC are most pronounced for Point 1 of the neat Cu sample (Fig. 5k), confirming a relatively large fraction of organic species compared to Point 2 on the neat Cu.[45] Interestingly, the Polymer@Cu samples show a very low contribution of Li_2CO_3, indicating that the carbonates formed (and detected in the O 1s spectra) are largely organic in nature. Since there is no clear signal of CF_3 at around 293.1 eV as a commonly expected decomposition product of LiTFSI, i.e., the conducting salt comprised in the PEO-based interlayer, it appears

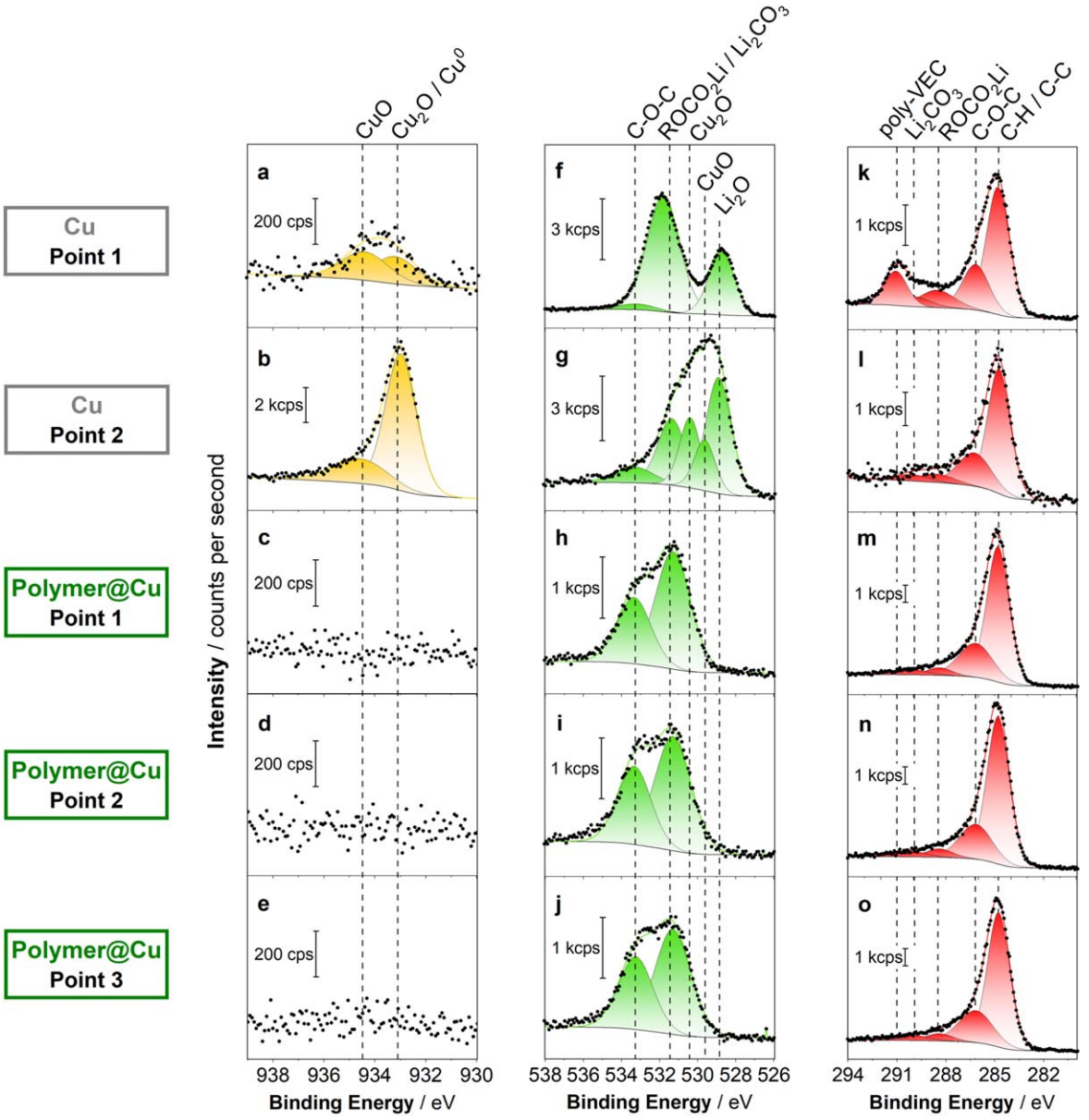

Figure 5. XPS detail spectra in the (a)–(e) Cu 2p, (f)–(j) O 1s and (k)–(o) C 1s region at the different measurement points on the Cu and Polymer@Cu sample (see Fig. S4).

that LiTFSI does not significantly contribute to the SEI composition.[48] Nevertheless, the presence of the TFSI anion in the PEO-based interlayer might still influence the lithium plating and stripping process, even though no evident contribution to the SEI composition was detected.[48,49]

The detail spectra for the Li 1s region are displayed in Figs. 6a–6e. While the spectra for all samples show a peak that was assigned to (organic) lithium carbonates along with other lithium compounds such as LiF (in fact, this peak covers a wide range of lithium compounds), the two spectra recorded for the neat Cu foil reveal an additional peak at 54.1 eV, which was attributed to Li_2O – in agreement with the O 1s data – which was not observed for the Polymer@Cu samples.[41,42] The presence of LiF is confirmed in the F 1s spectra for all samples (Figs. 6f–6j).[45] The amount of LiF at Point 1 and 2 of the neat Cu foil, however, is rather low and no other contributions from the salt decomposition were detected, in line with the findings from the P 2p spectra (Fig. S5), which indicates that the SEI on the neat Cu is dominated by decomposition products from the organic solvents. This observation would be in line with the inferior evolution of the Coulombic efficiency compared to the Polymer@Cu samples, as it has been commonly reported that a thin (but dense) inorganic and fluorine-rich inner SEI layer is crucial for lithium-metal electrodes in contact with liquid electrolyte systems.[16,45,50,51]

To complement the analysis of the sample surface, soft-XAS was performed, which allows for investigating different probing depths. In fact, while the information depth in the case of XPS is around 2–5 nm,[39] it is around 2–10 nm for soft-XAS in TEY mode at energies related to the elements of interest (Li—Cu), and in TFY mode it is around 100 nm.[52,53] Additionally, the soft-XAS beam was less focused, providing information over a much larger area. The normalized soft-XAS spectra for two areas on the Cu sample (in grey and black) and one area on the Polymer@Cu sample (in green) are displayed in Fig. 7. Figure 7a shows the carbon K-edge soft-XAS spectra collected in TEY mode. The spectra of the neat Cu sample exhibit two pronounced features: A sharp peak at 290.1 eV and a broader peak at around 300.0 eV, which can be ascribed to lithium carbonate, where the former corresponds to the C=O 1s-π^* and the latter to the C=O 1s-σ^* resonance.[52,54] The spectrum of the

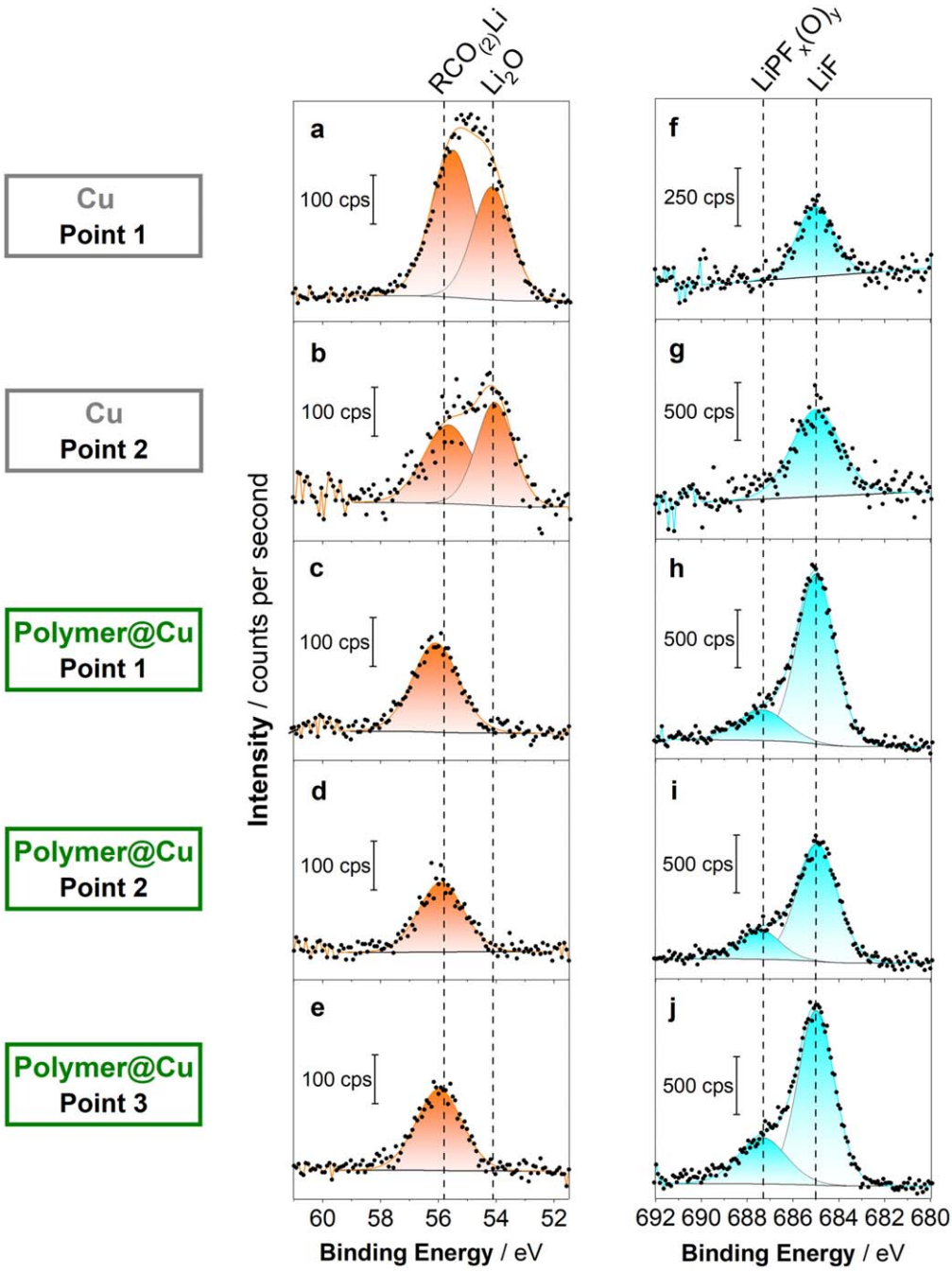

Figure 6. XPS detail spectra in the (a)–(e) the Li 1s and (f)–(j) F 1s region at the different measurement points on the Cu and Polymer@Cu sample (see Fig. S4).

Polymer@Cu sample does not show any absorption peak at the respective energies, which indicates that no excessive amounts of lithium carbonate are formed in the SEI—as also observed from the XPS analysis.

In Figs. 7b, 7c, the oxygen K-edge spectra recorded in TEY and TFY mode are presented. Similar to the carbon K-edge (Fig. 7a), the oxygen K-edge shows clear differences between the spectra of the current collectors that had or had not been modified by a polymer interlayer. The TEY and TFY spectra of the neat Cu sample (grey and black) show apparent features at 533.9 eV, 540.7 eV, and 544.2 eV, which can be assigned to the C=O 1s-π*, the C–O 1s-σ*, and the C=O 1s-σ* transition of Li_2CO_3, respectively.[54–57] The signal at 533.9 eV presumably also includes a contribution from Li_2O, since its absorption energy is expected at 534.0 eV.[58] This is in very good agreement with the XPS and SEM/EDX data. The more intense oxygen signal in the TFY spectrum of Position 1 presumably originates from even higher amounts of Li_2CO_3, as clear residues were visible at this spot by eye. In contrast, the spectrum of the Polymer@Cu sample (in green) does not exhibit clear peaks at the photon energies of Li_2CO_3, which confirms the results of the carbon K-edge spectra.

In Figs. 7d, 7e, the soft-XAS spectra recorded at the F K-edge are depicted. Both spectra of the neat Cu exhibit two (very) broad peaks at 689.0 eV and 694.6 eV, which can be attributed to the presence of P-F containing compounds, resulting from the decomposition of $LiPF_6$ and leading to the formation of, e.g., $Li_xPF_y(O)_z$.[54,58] The rather low overall intensities of the F spectra, especially in the TFY mode at Position 2, however, suggest that the SEI on the bare Cu current collector contains only little amounts of fluorine species. Besides, the absence of such signal and the detection of only a very

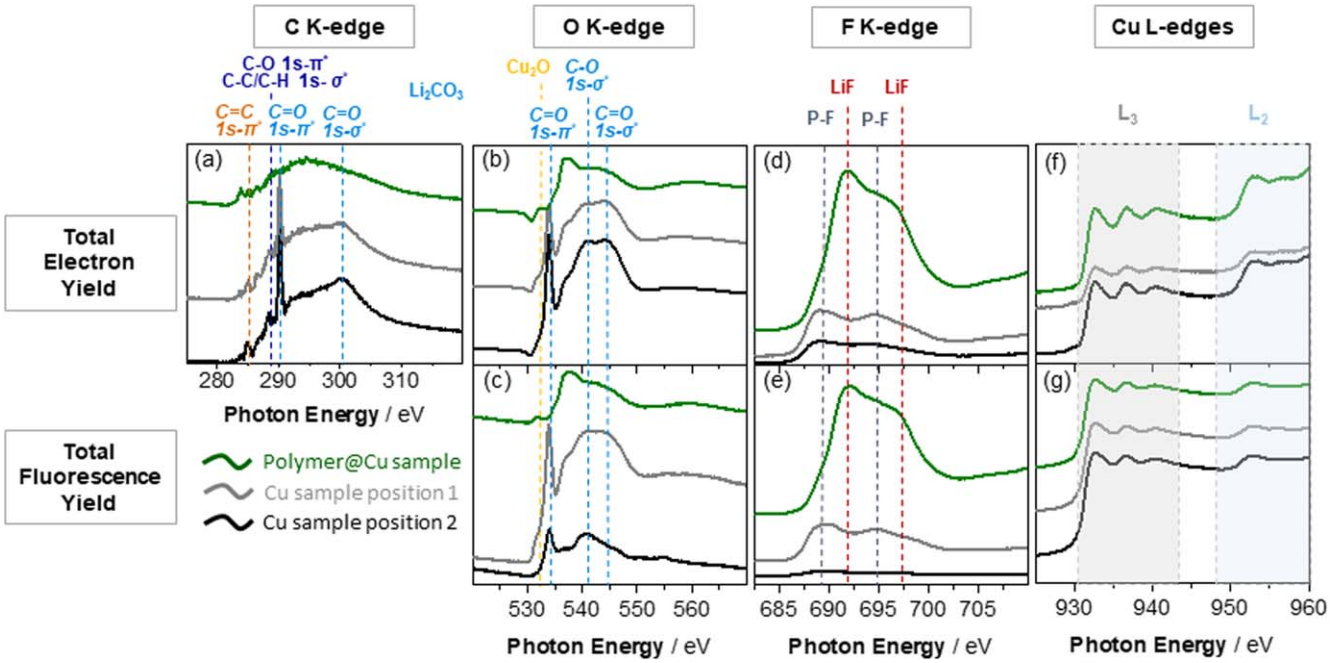

Figure 7. Soft-XAS spectra collected at (a) the C K-edge, (b), (c) the O K-edge, (d), (e) the F K-edge, and (f), (g) the Cu L-edges for a neat Cu current collector and Polymer@Cu after one plating/stripping cycle (1 mAh cm^{-2} at 0.5 mA cm^{-2}). The black spectra correspond to an area in the center of the Cu sample, the grey spectra to a position towards the edge of the Cu sample, and the green spectra to an area on the Polymer@Cu sample after polymer removal. The upper row shows soft-XAS spectra collected in the TEY mode and the lower row shows spectra collected in the TFY mode.

weak LiF-related peak in the XPS data suggests that these species are located more towards the inner part of the SEI, covered by organic decomposition products (keeping in mind the substantially greater probing depth of soft-XAS and the larger probing area). In the case of the Polymer@Cu sample, two broad peaks at 691.8 eV and 697.4 eV, related to the presence of LiF,[54,58] are dominating the spectrum. The great intensity of these features presumably superimposes the signals for P-F-comprising decomposition products, as also evidenced by the shoulder-like feature at about 689.0 eV. Generally, the comparison of the spectra further corroborates the finding that the SEI on the Polymer@Cu sample is substantially more LiF-enriched compared to the neat Cu samples, which is line with the XPS data.

The spectra in Figs. 7f, 7g show the typical Cu L_3 and L_2 absorption edges in all cases. At Position 1 on the neat Cu sample, the signal in TEY mode (Fig. 7f) is significantly lower than those observed in the other spectra, indicating the presence of a thicker layer of decomposition products on the Cu current collector, as also revealed by the comparison of the O K-edge spectra in Fig. 7c and the observation of residues at this position.

Conclusions

The application of a thin PEO-based artificial interphase on a copper current collector is beneficial for the reversibility of the lithium plating and stripping in organic carbonate-based liquid electrolytes, resulting in a stabilized and increased average Coulombic efficiency and denser lithium deposits. The thorough ex situ analysis via SEM/EDX, SPEM, XPS, and soft-XAS revealed that the use of a neat Cu current collector leads to the formation of inhomogeneously distributed lithium carbonate and lithium oxide as dominating inorganic electrolyte decomposition products, along with a relatively large contribution of organic species. These findings indicate that the decomposition of the organic carbonate solvents plays a major role for the SEI formation in this case. Differently, when introducing the PEO-based interlayer, the SEI is much richer in fluorinated species such as LiF, resulting from the decomposition of the conducting lithium salt. Additionally, the SEI is much more homogeneous in thickness and chemical composition in the presence of such a polymer interlayer, presumably as a result of the fluorine-rich interphase formed in combination with a more homogeneous lithium deposition. While the Coulombic efficiency still needs to be further increased to reach a practically suitable cycle life, e.g., by optimizing the composition of the polymer interlayer, the findings presented herein enable an enhanced understanding of the origin of such performance improvement and, thus, will hopefully contribute to the successful development of "zero excess" lithium-metal batteries in the future.

Acknowledgments

The authors would like to acknowledge financial support from the Federal Ministry of Education and Research (BMBF) within the HighSafe-II project (03XP0306C) and from the Helmholtz Association. We acknowledge Elettra Sincrotrone Trieste for providing access to its synchrotron radiation facilities, particularly the ESCA Microscopy and BEAR beamline.

ORCID

Dominic Bresser https://orcid.org/0000-0001-6429-6048

References

1. Y. Ding, Z. P. Cano, A. Yu, J. Lu, and Z. Chen, *Electrochem. Energ. Rev.*, **2**, 1 (2019).
2. D. Bresser, K. Hosoi, D. Howell, H. Li, H. Zeisel, K. Amine, and S. Passerini, *J. Power Sources*, **382**, 176 (2018).
3. Y. Yang, S. Bremner, C. Menictas, and M. Kay, *Renew. Sustain. Energy Rev.*, **91**, 109 (2018).
4. T. Placke, R. Kloepsch, S. Dühnen, and M. Winter, *J. Solid State Electrochem.*, **21**, 1939 (2017).
5. R. Schmuch, R. Wagner, G. Hörpel, T. Placke, and M. Winter, *Nat. Energy*, **3**, 267 (2018).
6. C.-J. Huang et al., *Nat. Commun.*, **12**, 1452 (2021).
7. Y. Tian, Y. An, C. Wei, H. Jiang, S. Xiong, J. Feng, and Y. Qian, *Nano Energy*, **78**, 105344 (2020).
8. C. Heubner, S. Maletti, H. Auer, J. Hüttl, K. Voigt, O. Lohrberg, K. Nikolowski, M. Partsch, and A. Michaelis, *Adv. Funct. Mater.*, **31**, 2106608 (2021).
9. X. Zhang, Y. Yang, and Z. Zhou, *Chem. Soc. Rev.*, **49**, 3040 (2020).
10. Z. Xie, Z. Wu, X. An, X. Yue, J. Wang, A. Abudula, and G. Guan, *Energy Storage Mater.*, **32**, 386 (2020).

11. J. Qian, B. D. Adams, J. Zheng, W. Xu, W. A. Henderson, J. Wang, M. E. Bowden, S. Xu, J. Hu, and J.-G. Zhang, *Adv. Funct. Mater.*, **26**, 7094 (2016).
12. S. Nanda, A. Gupta, and A. Manthiram, *Adv. Energy Mater.*, **11**, 2000804 (2021).
13. B. Horstmann et al., *Energy Environ. Sci.*, **14**, 5289 (2021).
14. M. Genovese, A. J. Louli, R. Weber, S. Hames, and J. R. Dahn, *J. Electrochem. Soc.*, **165**, A3321 (2018).
15. Z. Tong, B. Bazri, S.-F. Hu, and R.-S. Liu, *J. Mater. Chem. A*, **9**, 7396 (2021).
16. X. He et al., *Nature Reviews Materials*, **6**, 1036 (2021).
17. M. D. Tikekar, S. Choudhury, Z. Tu, and L. A. Archer, *Nat. Energy*, **1** (2016).
18. Z. Yu et al., *Nat. Energy*, **5**, 526 (2020).
19. S. Yuan, T. Kong, Y. Zhang, P. Dong, Y. Zhang, X. Dong, Y. Wang, and Y. Xia, *Angew. Chem.*, **133**, 25828 (2021).
20. N. A. Sahalie, A. A. Assegie, W.-N. Su, Z. T. Wondimkun, B. A. Jote, B. Thirumalraj, C.-J. Huang, Y.-W. Yang, and B.-J. Hwang, *J. Power Sources*, **437**, 226912 (2019).
21. Y. Yang, J. Xiong, S. Lai, R. Zhou, M. Zhao, H. Geng, Y. Zhang, Y. Fang, C. Li, and J. Zhao, *ACS Appl. Mater. Interfaces*, **11**, 6118 (2019).
22. T. M. Hagos et al., *Electrochim. Acta*, **316**, 52 (2019).
23. H. Zhang, G. G. Eshetu, X. Judez, C. Li, L. M. Rodriguez-Martínez, and M. Armand, *Angew. Chem. Int. Ed.*, **57**, 15002 (2018).
24. S. Jiao et al., *Nat. Energy*, **3**, 739 (2018).
25. R. Weber, M. Genovese, A. J. Louli, S. Hames, C. Martin, I. G. Hill, and J. R. Dahn, *Nat. Energy*, **4**, 683 (2019).
26. Y. Liu, D. Lin, Z. Liang, J. Zhao, K. Yan, and Y. Cui, *Nat. Commun.*, **7**, 10992 (2016).
27. L.-L. Lu, J. Ge, J.-N. Yang, S.-M. Chen, H.-B. Yao, F. Zhou, and S.-H. Yu, *Nano Lett.*, **16**, 4431 (2016).
28. C.-P. Yang, Y.-X. Yin, S.-F. Zhang, N.-W. Li, and Y.-G. Guo, *Nat. Commun.*, **6**, 8058 (2015).
29. D. Kang, M. Xiao, and J. P. Lemmon, *Batteries & Supercaps*, **4**, 445 (2021).
30. R. Xu, X.-B. Cheng, C. Yan, X.-Q. Zhang, Y. Xiao, C.-Z. Zhao, J.-Q. Huang, and Q. Zhang, *Matter*, **1**, 317 (2019).
31. A. A. Assegie, C.-C. Chung, M.-C. Tsai, W.-N. Su, C.-W. Chen, and B.-J. Hwang, *Nanoscale*, **11**, 2710 (2019).
32. Z. Yu, Y. Cui, and Z. Bao, *Cell Reports Physical Science*, **1**, 100119 (2020).
33. K. Liu et al., *JACS*, **139**, 4815 (2017).
34. A. A. Assegie, J.-H. Cheng, L.-M. Kuo, W.-N. Su, and B.-J. Hwang, *Nanoscale*, **10**, 6125 (2018).
35. S. Passerini, D. Bresser, A. Moretti, and A. Varzi, *Batteries: Present and Future Energy Storage Challenges* (Wiley, New York, NY) (2020).
36. Z. Xue, D. He, and X. Xie, *J. Mater. Chem. A*, **3**, 19218 (2015).
37. G. T. Kim, G. B. Appetecchi, M. Carewska, M. Joost, A. Balducci, M. Winter, and S. Passerini, *J. Power Sources*, **195**, 6130 (2010).
38. M. Falco, C. Simari, C. Ferrara, J. R. Nair, G. Meligrana, F. Bella, I. Nicotera, P. Mustarelli, M. Winter, and C. Gerbaldi, *Langmuir: the ACS journal of surfaces and colloids*, **35**, 8210 (2019).
39. S. Oswald and R. Reiche, *Appl. Surf. Sci.*, **179**, 307 (2001).
40. T. H. Fleisch and G. J. Mains, *Appl. Surf. Sci.*, **10**, 51 (1982).
41. I. Weber, J. Schnaidt, B. Wang, T. Diemant, and R. J. Behm, *ChemElectroChem*, **6**, 4985 (2019).
42. S. Tanaka, M. Taniguchi, and H. Tanigawa, *J. Nucl. Mater.*, **283–287**, 1405 (2000).
43. R. P. Vasquez, *Surf. Sci. Spectra*, **5**, 262 (1998).
44. R. P. Vasquez, *Surf. Sci. Spectra*, **5**, 257 (1998).
45. V. Sharova, A. Moretti, T. Diemant, A. Varzi, R. Behm, and S. Passerini, *J. Power Sources*, **375**, 43 (2018).
46. J. A. Rotole and P. M. A. Sherwood, *Surf. Sci. Spectra*, **5**, 60 (1998).
47. M. Steinhauer, T. Diemant, C. Heim, R. Jürgen Behm, N. Wagner, and K. Andreas Friedrich, *J. Appl. Electrochem.*, **47**, 249 (2017).
48. W. Fan, N.-W. Li, X. Zhang, S. Zhao, R. Cao, Y. Yin, Y. Xing, J. Wang, Y.-G. Guo, and C. Li, *Adv. Sci.*, **5**, 1800559 (2018).
49. Z. K. Liu, J. Guan, H. X. Yang, P. X. Sun, N. W. Li, and Le Yu, *Chem. Commun.*, **58**, 10973 (2022).
50. M. He, R. Guo, G. M. Hobold, H. Gao, and B. M. Gallant, *PNAS*, **117**, 73 (2020).
51. J. Luo, C.-C. Fang, and N.-L. Wu, *Adv. Energy Mater.*, **8**, 1701482 (2018).
52. A. Di Cicco, A. Giglia, R. Gunnella, S. L. Koch, F. Mueller, F. Nobili, M. Pasqualini, S. Passerini, R. Tossici, and A. Witkowska, *Adv. Energy Mater.*, **5**, 1500642 (2015).
53. M. Kasrai, W. N. Lennard, R. W. Brunner, G. M. Bancroft, J. A. Bardwell, and K. H. Tan, *Appl. Surf. Sci.*, **99**, 303 (1996).
54. T. Eisenmann, J. Asenbauer, S. J. Rezvani, T. Diemant, R. J. Behm, D. Geiger, U. Kaiser, S. Passerini, and D. Bresser, *Small Methods*, **5**, e2001021 (2021).
55. F. Frati, M. O. J. Y. Hunault, and F. M. F. de Groot, *Chem. Rev.*, **120**, 4056 (2020).
56. S. J. Rezvani, F. Nobili, R. Gunnella, M. Ali, R. Tossici, S. Passerini, and A. Di Cicco, *J. Phys. Chem. C*, **121**, 26379 (2017).
57. S. J. Rezvani, R. Gunnella, A. Witkowska, F. Mueller, M. Pasqualini, F. Nobili, S. Passerini, and A. Di Cicco, *ACS Appl. Mater. Interfaces*, **9**, 4570 (2017).
58. R. Qiao, I. T. Lucas, A. Karim, J. Syzdek, X. Liu, W. Chen, K. Persson, R. Kostecki, and W. Yang, *Adv. Mater. Interfaces*, **1**, 1300115 (2014).